Along-axis variation in crustal thickness at the ultraslow spreading Southwest Indian Ridge (50°E) from a wide-angle seismic experiment

Xiongwei Niu, Aiguo Ruan, Jiabiao Li, T.A. Minshull, Daniel Sauter, Zhenli Wu, Xuelin Qiu, Minghui Zhao, John Chen, Satish Singh

AGU PUBLICATIONS

Geochemistry, Geophysics, Geosystems

RESEARCH ARTICLE
10.1002/2014GC005645

Key Points:
- A 10.2 km thick crust at ultraslow spreading ridge
- An abrupt along-axis change in crustal thickness between SWIR segments 28 and 27
- Normal mantle velocity

Correspondence to:
A. Ruan,
ruanag@163.com

Citation:
Niu, X., A. Ruan, J. Li, T. A. Minshull, D. Sauter, Z. Wu, X. Qiu, M. Zhao, Y. J. Chen, and S. Singh (2015), Along-axis variation in crustal thickness at the ultraslow spreading Southwest Indian Ridge (50°E) from a wide-angle seismic experiment, *Geochem. Geophys. Geosyst.*, *16*, 468–485, doi:10.1002/2014GC005645.

Received 5 NOV 2014
Accepted 20 JAN 2015
Accepted article online 28 JAN 2015
Published online 19 FEB 2015

Along-axis variation in crustal thickness at the ultraslow spreading Southwest Indian Ridge (50°E) from a wide-angle seismic experiment

Xiongwei Niu[1], Aiguo Ruan[1], Jiabiao Li[1], T. A. Minshull[2], Daniel Sauter[3], Zhenli Wu[1], Xuelin Qiu[4], Minghui Zhao[4], Y. John Chen[5], and Satish Singh[6]

[1]Second Institute of Oceanography, State Oceanic Administration, Hangzhou, China, [2]Ocean and Earth Science, National Oceanography Centre Southampton, University of Southampton, Southampton, UK, [3]Institut de Physique du Globe de Strasbourg, IPGS-UMR 7516, CNRS, Université de Strasbourg/EOST, Strasbourg, France, [4]South China Sea Institute of Oceanology, Chinese Academy of Sciences, Guangzhou, China, [5]Department of Geophysics, School of Earth and Space Sciences, Peking University, Beijing, China, [6]Laboratoire de Géosciences Marines, Institut de Physique du Globe de Paris, Paris, France

Abstract The Southwest Indian Ridge (SWIR) is characterized by an ultraslow spreading rate, thin crust, and extensive outcrops of serpentinized peridotite. Previous studies have used geochemical and geophysical data to suggest the presence of a thicker crust at the central and shallowest portions of the SWIR, from the Prince Edward (35°30′E) to the Gallieni (52°20′E) fracture zones. Here we present a new analysis of wide-angle seismic data along the ridge 49°17′E–50°49′E. Our main conclusions are as follows: (1) we find an oceanic layer 2 of roughly constant thickness and steep velocity gradient, underlain by a layer 3 with variable thickness and low velocity gradient; (2) the crustal thickness varies from ~5 km beneath nontransform discontinuities (NTDs) up to ~10 km beneath a segment center; (3) the melt supply is focused in segment centers despite a small NTD between adjacent segments; (4) the presence of a normal upper mantle velocity indicates that no serpentinization occurs beneath this thick crust. Our observation of thick crust at an ultraslow spreading ridge adds further complexity to relationships between crustal thickness and spreading rate, and supports previous suggestions that the extent of mantle melting is not a simple function of spreading rate, and that mantle temperature or chemistry (or both) must vary significantly along axis.

1. Introduction

The oceanic crust exhibits a remarkably uniform thickness (6–7 km) across almost the entire spreading rate range [*White et al.*, 2001]. Total crustal production, away from hot spots and fracture zones, does not depend on the spreading rate, with the exception of the slowest end of the spreading-rate spectrum [*Bown and White*, 1994]. Fifty years ago it was suggested that the seismic crustal thickness drops off rapidly (2–4 km) below spreading rates of 20 mm/yr [*Raitt*, 1963]. Below this critical spreading rate, the melt supply per increment of plate separation is predicted to decrease dramatically due to a thickening of the thermal boundary layer by conductive cooling of the slow upwelling mantle [*Reid and Jackson*, 1981]. Therefore, slow spreading ridges have formed a focus for the study of the effects of ridge geometry, mantle composition, and thermal structure on crustal production [e.g., *Cannat et al.*, 2006, 2008; *Dick et al.*, 2003; *Standish et al.*, 2008]. In particular, "amagmatic spreading segments" have been proposed to exist on ultraslow spreading ridges such as the Southwest Indian Ridge (SWIR), and it has been argued that these ridge segments represent a previously unrecognized class of plate boundary structure [*Dick et al.*, 2003]. Along the SWIR, amagmatic segments expose mantle peridotite rocks directly on the seafloor, with only scattered basalt and gabbro along the ridge axis [*Dick et al.*, 2003; *Sauter et al.*, 2004], as well as on the flanks [*Cannat et al.*, 2006; *Sauter et al.*, 2013].

To date, studies of axial crustal structure have been focused mostly on deep melt-poor ridge sections [e.g., *Minshull et al.*, 2006; *Muller et al.*, 1997] and little attention has been given to the central and shallowest portions of the SWIR, from the Prince Edward (35°30′E) to the Gallieni (52°20′E) fracture zones (FZs; Figure 1),

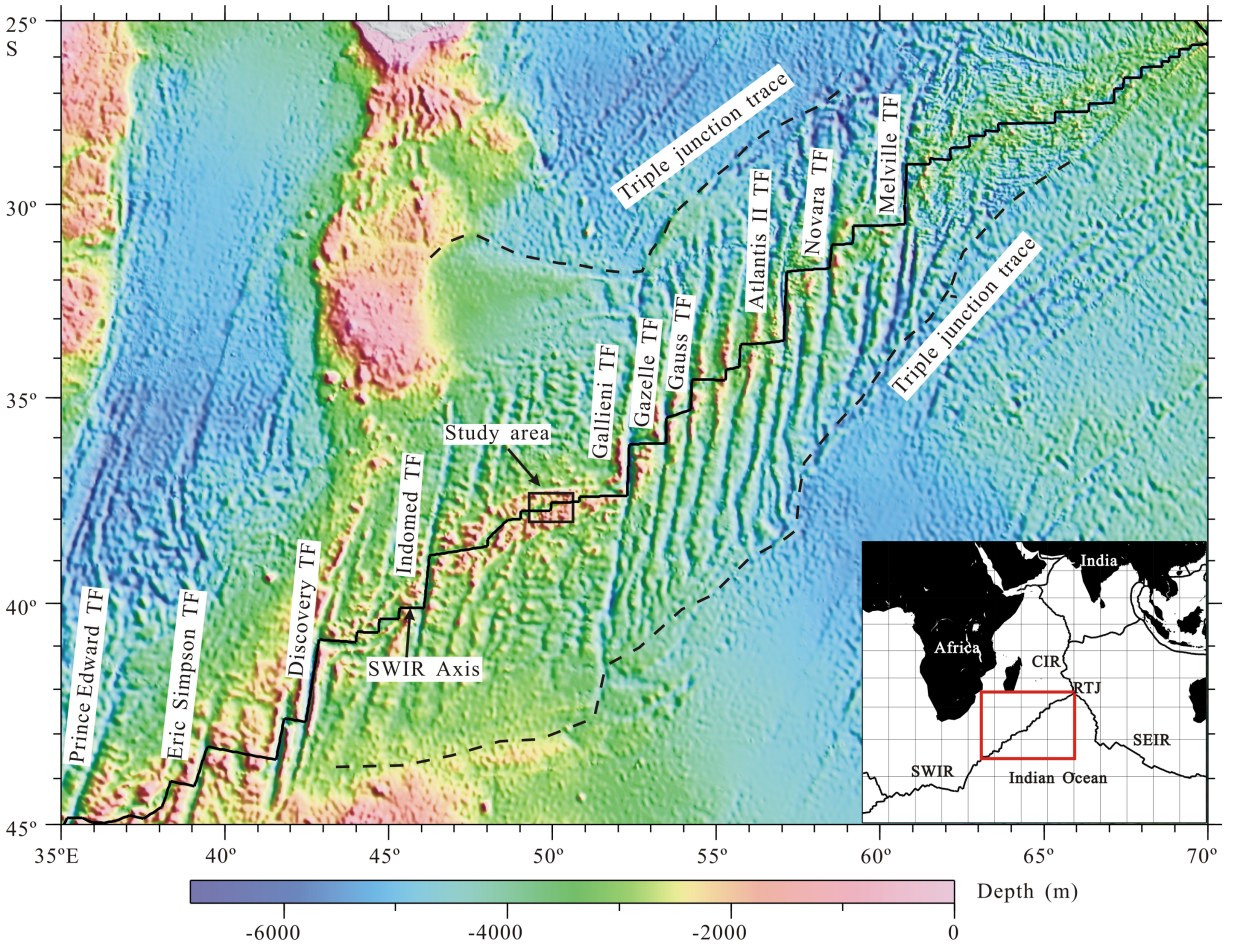

Figure 1. Bathymetric map of the shallow central portion of the SWIR derived from ETOPO1V1. The black rectangle indicates the research area. The black solid line represents the ridge axis with the major transform faults labeled. The inset indicates the global location of Figure 1.

where geochemical and geophysical data suggest the presence of a thicker crust [*Georgen et al.*, 2001; *Sauter et al.*, 2009]. Both the extent of crustal thickening and the mechanism responsible for it are debated. Based on the composition of dredge samples, *Zhou and Dick* [2013] argued for a thin crust in this region (~2 km), related to a compositional anomaly in the underlying mantle, and challenged the prevailing view that variations in depth of spreading ridges is controlled by the temperature of the underlying mantle. In contrast, a much thicker crust (>6 km) has been inferred from mantle Bouguer anomaly (MBA) calculations [*Sauter et al.*, 2009; *Zhang et al.*, 2011] and the sodium content of dredged basalts [*Cannat et al.*, 2008], consistent at the larger extent of melting controlled by hotter mantle temperatures. Both gravity and geochemical data are influenced by mantle properties, and neither can constrain uniquely crustal thickness/melt production. Wide-angle seismic data were, therefore, crucially needed within the shallow central portion of the SWIR in order to constrain crustal thickness estimates and to aid the understanding of the thermal state of the mantle along the SWIR.

On a smaller scale, an analysis of the shallow central section of the SWIR has revealed that the segmentation defined by axial depth variations, and the occurrence of axial offsets, does not correspond systematically to the segmentation defined by along-axis variations of other geophysical measurements such as the backscattering strength, the MBA, and the amplitude of central magnetic anomalies [*Sauter et al.*, 2001]. Since small variations in volcanic production and crustal thickness appear to be associated with small axial discontinuities (offset <15 km) between low-relief segments and high relief segments, it has been suggested that the magma supply to these low-relief segments is controlled by near-surface processes such as crustal melt migration from adjacent magmatically robust segments [*Sauter et al.*, 2001]. Additional direct observations such as those provided by deep crustal seismic data are needed to test these interpretations and to help us

to understand magma budget variations and magma distribution along ultraslow spreading ridges [*Sauter and Cannat*, 2010].

In February 2010, we conducted a 3-D wide-angle seismic experiment [*Li and Chen*, 2010; *Zhao et al*., 2013] by deploying an array of forty ocean bottom seismometers (OBSs) on the ridge section between 49°17′E and 50°49′E during the Chinese DY115-21 cruise (Leg 6) in order to determine the crustal structure beneath the shallow central ridge section. The experiment was located on ridge segments 27–29, as defined by *Cannat et al*. [1999]. *Zhao et al*. [2013] have presented a three-dimensional analysis of segment 28 based on first arrival travel time inversion only. Here we analyze a well-sampled profile that traverses both segments and the NTDs at the ends of segment 28, using both first arrivals and wide-angle reflections. We determine the crustal thickness and the velocity structure beneath the segments and NTDs. Based on the resulting velocity model, we discuss the characteristics and the formation mechanism of the thick crust, and the role of magma supply along the SWIR.

2. Regional Setting

The SWIR is among the world's slowest spreading ridges, with an almost constant full spreading rate of ∼14 mm/yr along the 7700 km ridge axis [*Chu and Gordon*, 1999]. The compilation of bathymetric data along the axial valley revealed a shallow central region between the Prince Edward and Gallieni TFs, with an average depth of ∼3200 m relative to the deeper western (∼4000 m) and easternmost (∼4500 m) portions of the ridge [*Sauter et al*., 2001; *Cannat et al*., 2008]. Regional averages for axial depth along long portions (>200 km) of the SWIR are well correlated with axial values of the MBA, averaged over the same regions [*Cannat et al*., 2008], indicating that regional axial depths are related to the density structure of the ridge axis. Shallow axial depths and regional low MBA values between the Prince Edward and Gallieni TFs also correlate with regional low averages of the Na_8 content (Na corrected for fractional crystallization) [*Cannat et al*., 2008] in dredged basalts. Nevertheless, numerous exposures of mantle peridotite and the sparseness of gabbro have led some authors to challenge the idea of a purely thermal origin for this region [*Zhou and Dick*, 2013]. Indeed, *Zhou and Dick* [2013] argued for a generally thin and often missing crust, and suggested that the shallow bathymetry is supported by a highly depleted buoyant mantle rather than a hot mantle plume.

The area discussed here lies between the Indomed (46°E) and Gallieni TFs (52°20′E), in the central shallow portion of the SWIR. This ridge section has an overall 15° obliquity and is devoid of transform faults. Anomalously shallow ridge flanks suggest that this area has experienced a dramatic increase in magma supply since 8–10 Ma [*Sauter et al*., 2001, 2004] and that it is characterized by robust magmatism with abundant basalt at the seabed [*Sauter et al*., 2004], and without peridotites [*Zhou and Dick*, 2013]. The ridge section between segments 29 and 28 consists of a 19.5 km long NTD with a strike of N80°E and an offset of 15 km, with axial depths of ∼4 km. Here the distance between the axial valley walls is ∼10 km. To the east of the NTD, segment 28 is marked by an east-west-trending 27 km long axial volcanic ridge, with the Dragon Flag active hydrothermal field nearby [*Tao et al*., 2011, 2012]. The axial depth in this segment becomes shallower than 3 km and the ridge valley narrows to 5 km. East of segment 28, in a 10 km long NTD, both the valley width and the water depth again increase. In the 72 km long segment 27, the axial depth decreases below 2 km and an inactive hydrothermal vent field [*Tao et al*., 2012] is located in the segment center. Here numerous volcanic edifices are present on both flanks of the axial valley, with relatively flat topography to the north and greater relief to the south. The residual MBA suggests that the crustal thickness is 5–6 km in segment 28 and an average of 7.2 km in segment 27, with a maximum of 8 km [*Sauter et al*., 2004, 2009]. Even larger values (up to 9.0 km) were inferred by *Zhang et al*. [2013] from satellite-derived gravity anomalies. The apparent anomalously thick oceanic crust indicates that the magma supply in this area is robust and may be associated with a hot spot [*Sauter et al*., 2009; *Zhang et al*., 2013]. Indeed, on the Antarctic plate to the south, there are several oceanic plateaus including the Marion Plateau, the Del Cano Rise, and the Crozet Plateau. The associated melting anomalies are thought to influence strongly the magmatism, spreading process, and tectonic structure of a broad region of the SWIR [*Zhou and Dick*, 2013; *Zhang et al*., 2011; *Muller et al*., 1993; *Storey et al*., 1995; *Goslin and Diament*, 1987; *Recq et al*., 1998; *Mahoney et al*., 1996; *Curray and Munasinghe*, 1991; *Sauter et al*., 2009].

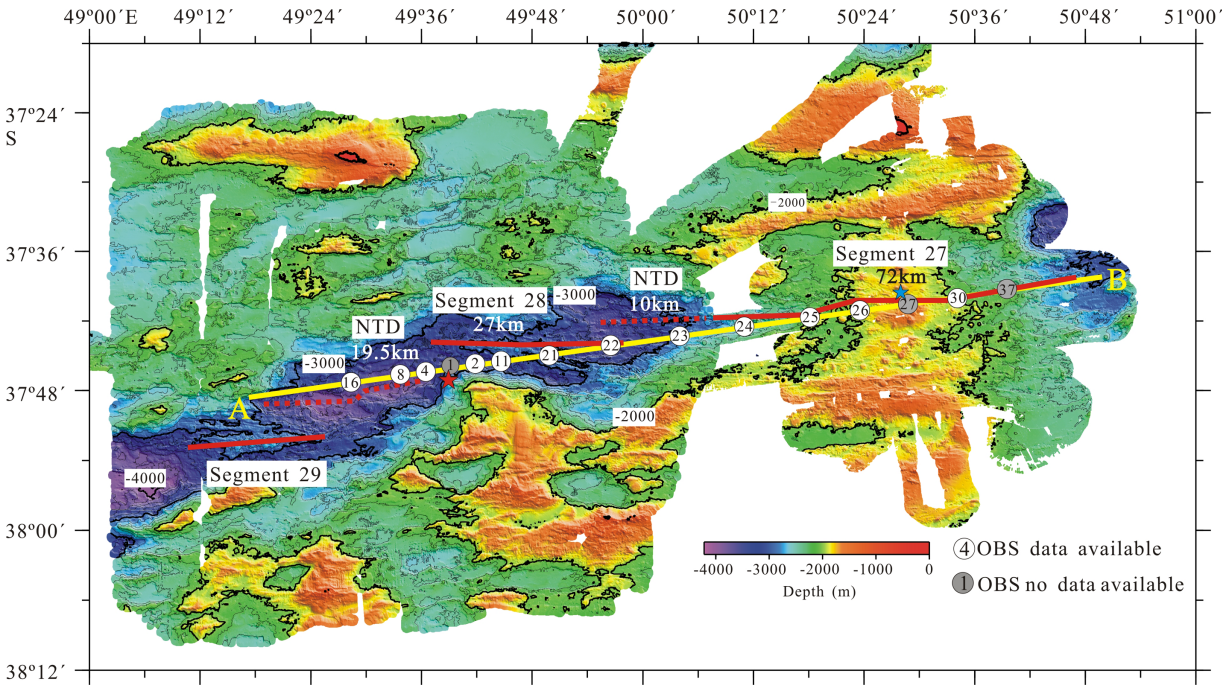

Figure 2. Bathymetry map of the research area derived from the multibeam data acquired by the Chinese R/V *Dayang Yihao*. The solid yellow line indicates the seismic profile. The numbers in white circles on the line indicate the OBS stations. The red solid and dashed lines indicate the spreading segments and the NTDs respectively [*Cannat et al.*, 1999; *Sauter et al.*, 2001]. The red star represents the Dragon Flag active vent field discovered by the Dayang Yihao in 2007 [*Tao et al.*, 2012]. The blue star represents an inactive hydrothermal vent [*Tao et al.*, 2012].

3. OBS Data

3.1. Data Acquisition

The seismic source was a 4 × 24.5 L air-gun array shot at a pressure of 10.79 MPa every 80–120 s, giving an average shooting interval of 200–300 m. Here we focus on one 138 km seismic profile with 596 shots (labeled AB in Figure 2), on which data were successfully recorded on 12 OBS, each recording four components sampled every 4 ms.

3.2. Data Processing

The processing of OBS data included correction for OBS clock drift, relocation of OBSs and shots using direct arrivals, and band-pass filtering at 4–20 Hz [*Ao et al.*, 2010]. During OBS relocation, the OBS depth best fitting the direct arrivals was also calculated, and the final OBS depth was refined using multibeam bathymetric data. Due to the high quality of navigation and bathymetric data, we were able by this process to fit water wave picks within 20 ms. A final straight-line approximation of the profile was determined by a least squares fit to all the shots on the profile.

3.3. Phase Analysis and Selection

In general, the seismic data quality is high. Phases were identified using initial travel time modeling of the vertical geophone component, and the details of the initial model are described in section 4.1. We identified the direct water wave labeled Pw, the refracted wave from oceanic layers 2A, 2B, and 3 labeled P1, P2, and P3, respectively, the Moho reflection labeled PmP, and the refracted wave from the upper mantle labeled Pn.

Phases P1 (recorded by 5 OBSs), P2 (recorded by 12 OBSs), P3 (recorded by 12 OBSs), PmP (recorded by 9 OBSs), and Pn (recorded by 7 OBSs) were observed, and Pn was observed to a maximum offset of 70 km. PmP appears at 17 km offset to the west of OBS30 (Figure 3), but mantle arrivals do not become first arrivals, providing evidence for thick crust beneath segment 27. PmP phases appear at 12 km offset west and 35 km offset east of OBS24 (Figure 4), with a weak Pn phase to the west. This strong asymmetry provides evidence for a large change in crustal thickness in the vicinity of OBS24. OBS23 shows a similar asymmetry

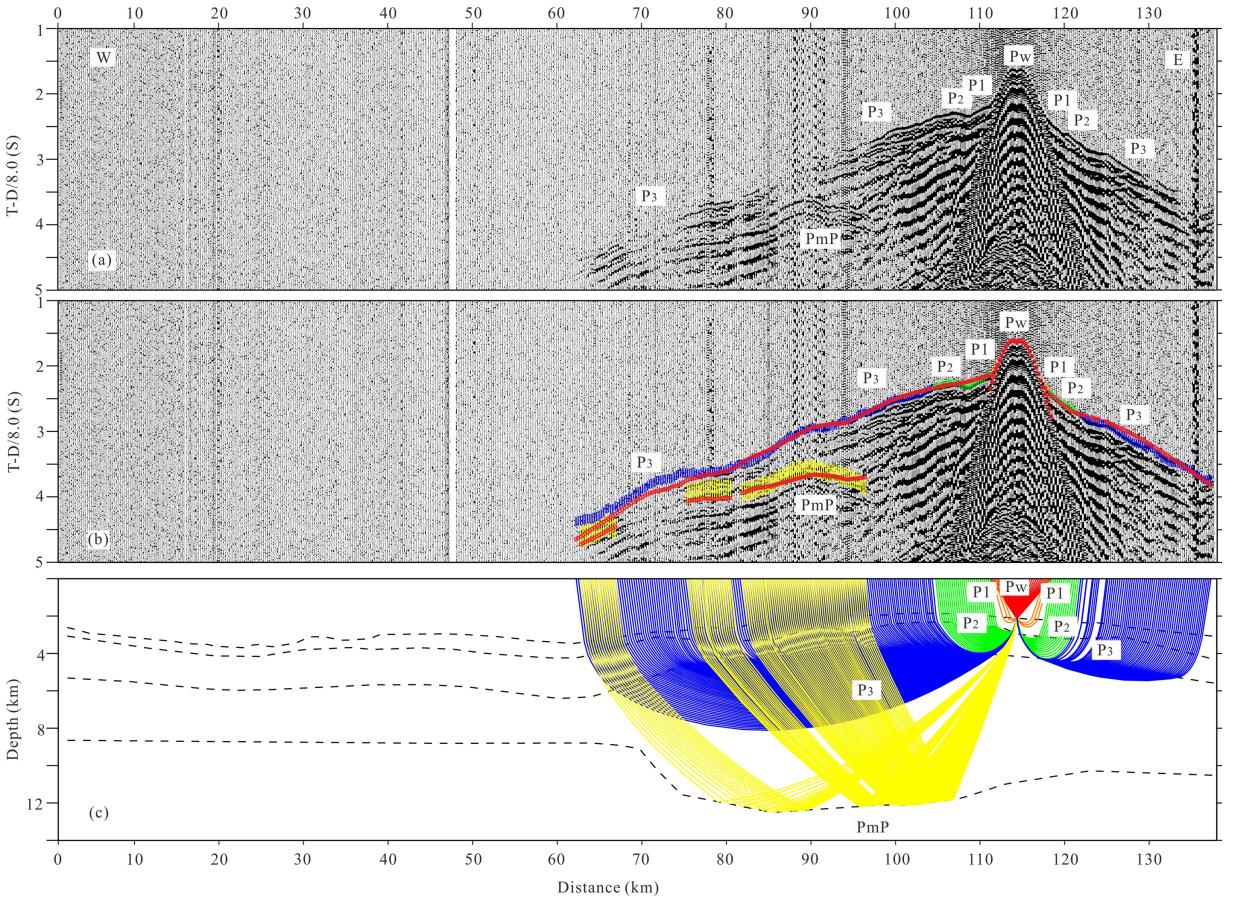

Figure 3. (a) A record section of the vertical component of OBS 30 on profile AB, (b) the record section with picked and calculated travel-times overlain, and (c) corresponding ray diagram. In these diagrams the reduction velocity is 8.0 km/s. The phase labels are explained in the text. In (b), red dots represent the predicted travel time and the colored vertical bars correspond to the rays in (c). The size of the vertical bars indicates twice the pick uncertainty [*Zelt and Smith*, 1992]. In (c), the colored lines represent the ray paths of different phases and the black dashed lines represent the seabed, the interface between oceanic layer 2A and layer 2B, layer 2B and layer 3, and the Moho discontinuity respectively, from top to bottom.

(Figure 5), with a pronounced PmP phase appearing 10 km to the west and 25 km to the east, and a weak Pn phase to the west only. Data from OBS4, at the end of segment 28, are more enigmatic (Figures 6 and 7). PmP appears at 25 km and Pn may be traced to a maximum offset of 70 km. However, a model with thin crust beneath segment 28, that provides a good fit to data from OBSs deployed on segment 27, provides a poor fit to these Pn arrivals (Figure 6). A better fit is achieved if the crustal thickness beneath segment 28 is increased by about 1.5 km (Figure 7). We infer that in the vicinity of this OBS, a two-dimensional model is inadequate. We note that *Zhao et al*. [2013] observe a small region of thickened crust just to the north of OBS2 and OBS11, and speculate that Pn arrivals from OBS4 are sampling this thicker crust.

4. Results

4.1. Modeling Approach

Our initial model consisted of four crustal layers, as follows: (1) oceanic layer 2A with 0.5 km thickness and with velocities of 1.8 km/s at the top and 3.4 km/s at the bottom; (2) oceanic layer 2B with 1.5 km thickness and velocities of 4.8 km/s at the top and 6.4 km/s at the bottom; (3) oceanic layer 3 with 4 km thickness and velocities of 6.4 km/s at the top and 7.0 km/s at the bottom; and (4) the upper mantle with velocities of 8.0 km/s at the top. This model is based on global averages of oceanic crustal structure [*Kennett*, 1982; *White et al*., 1992] and seismic velocity models of the SWIR at 66°E and 57°E [*Muller et al*., 1997, 1999, 2000; *Minshull et al*., 2006]. Two-dimensional velocity models were parameterized as sheared meshes beneath the seafloor. The initial horizontal velocity node spacings within oceanic layers 2A, 2B, and 3 were 5, 5, and 10 km, respectively. In the upper mantle, node spacing was 40 km. The vertical node spacing was set to the

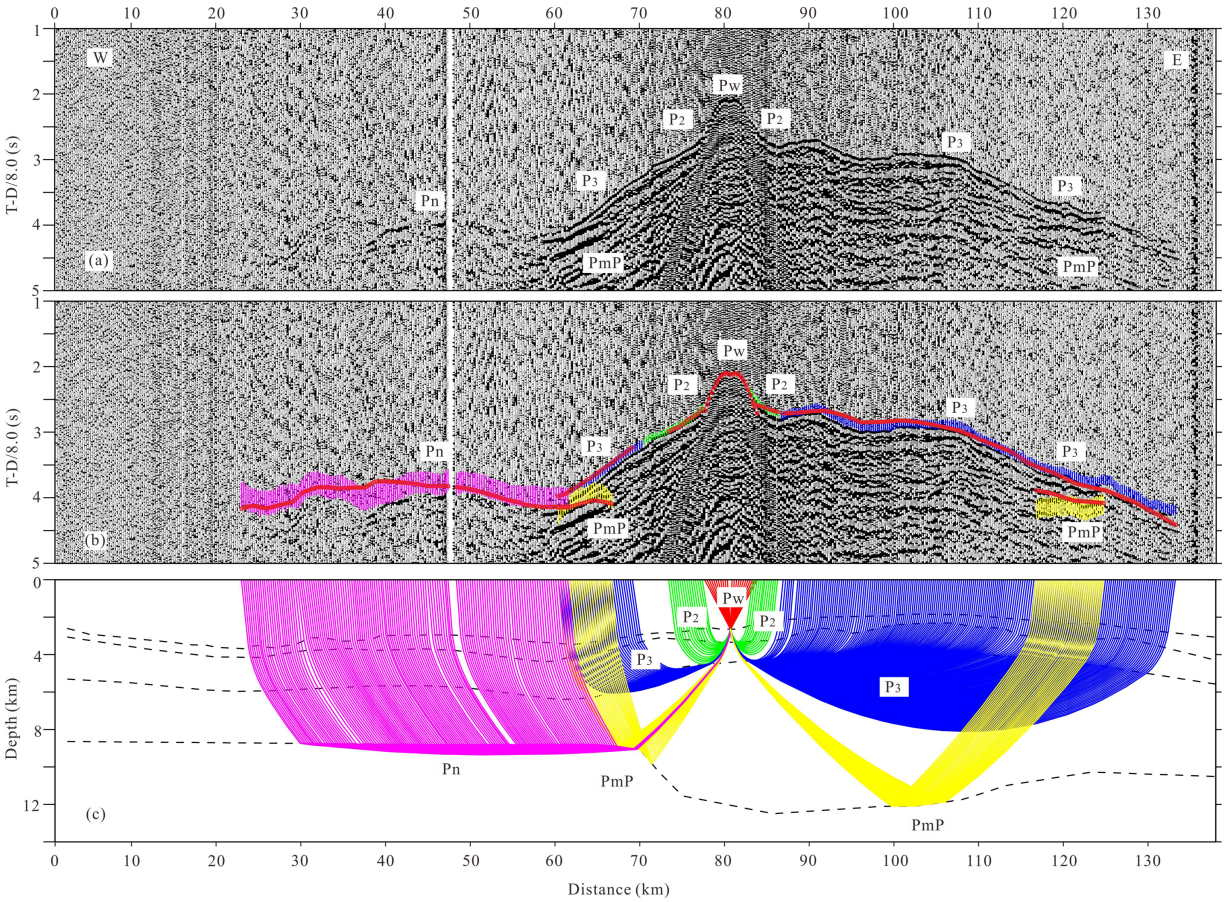

Figure 4. (a) A record section of the vertical component of OBS 24 on profile AB, (b) the record section with picked and calculated travel-times overlain, and (c) ray diagram.

layer thickness in order to maintain a constant vertical velocity gradient within each layer. Velocity models were constructed by two-dimensional travel time modeling and inversion using the RayInvr code of *Zelt and Smith* [1992]. Velocities and boundaries were initially adjusted manually by trial and error. Node spacings in sparsely sampled parts of the model were increased to ensure that most parameters had a resolution value defined by this code of greater than 0.5 (see below). After this forward modeling, a damped least squares inversion was conducted in order to optimize the velocity within each layer, while keeping the layer boundaries fixed.

4.2. The Velocity Model of Profile AB

Information regarding the travel time fit achieved for profile AB is given in Table 1. We obtained two versions of the final velocity model (Figure 8), but based on the analysis at the end of section 3.3 above we focus our interpretation on the model with thinner crust beneath segment 28. Our model indicates that major changes in crustal structure are accommodated by large variations in the thickness of oceanic layer 3 and Moho depth, while oceanic layer 2 has a more constant thickness. The data require lateral velocity variation only in layer 2A and at the top of layer 2B; there is no evidence for lateral velocity variation in the bottom of layer 2B, in layer 3 or in the upper mantle. The vertical velocity gradient within layer 2 was large (up to 2.49/s). In general, the velocity model is consistent with the morphologically defined segmentation of the ridge [*Sauter et al.*, 2001]. The most striking feature of the model is the large crustal thickness (up to 10 km) beneath segment 27, which is much larger than the 2.5–4.5 km typically observed for ultraslow spreading ridges [*White et al.*, 2001], and even larger than the mean thickness of normal oceanic crust elsewhere (6.3 $\pm$ 0.9 km) [*White et al.*, 2001].

Beneath the NTD between segments 29 and 28 (model distances up to 29 km), layers 2A and 2B have roughly constant thickness (around 0.5 and 1.8 km, respectively), and large vertical velocity gradients

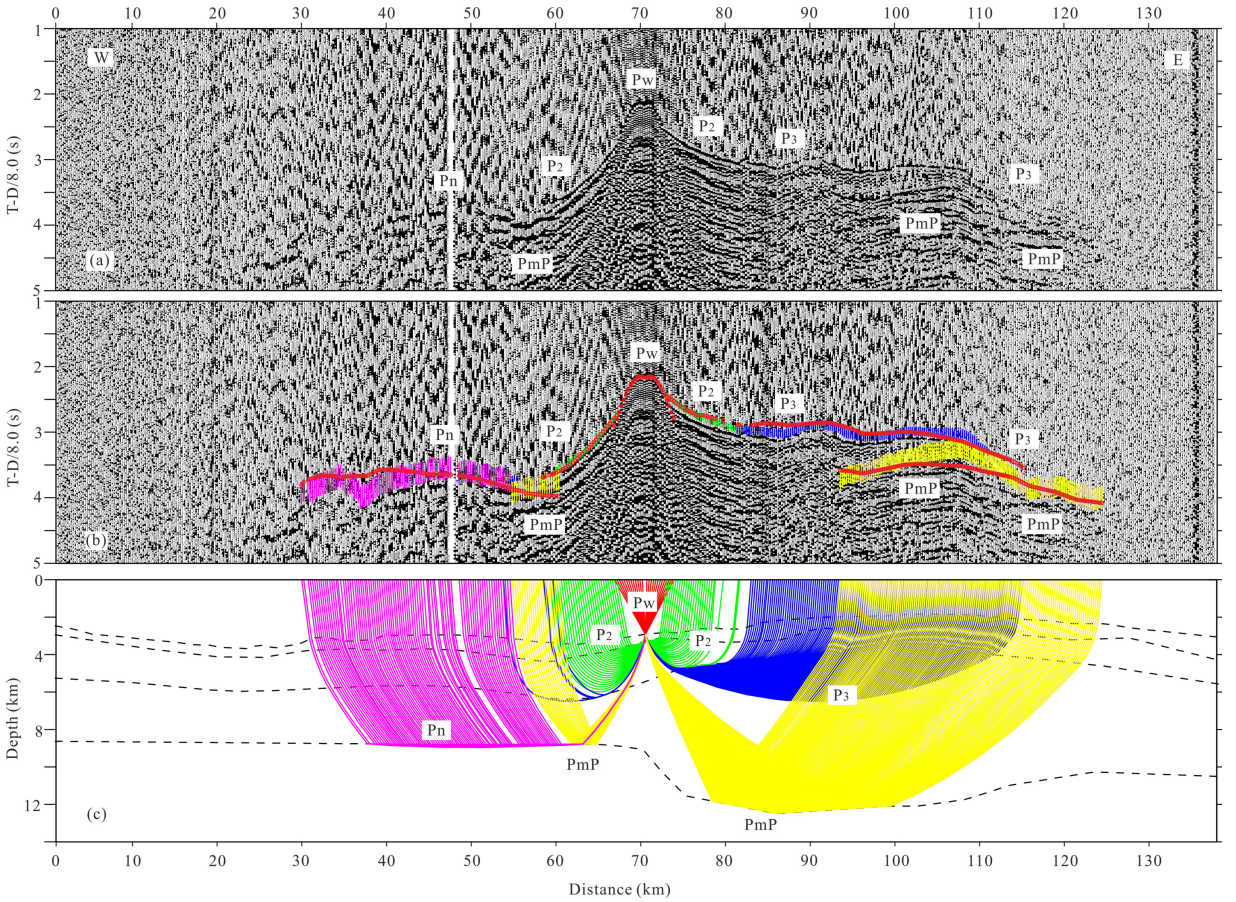

Figure 5. (a) A record section of the vertical component of OBS 23 on profile AB, (b) the record section with picked and calculated travel-times overlain, and (c) ray diagram.

(∼2.9/s and ∼1.3/s, respectively). Layer 3 is ∼2.8 km thick, on average, with a vertical velocity gradient of 0.2/s. Here the Moho lies at ∼8.6 km below sea level (bsl), resulting in a crustal thickness of 5.2 km, though constraints on crustal thickness are weak directly beneath the NTD because of the absence of PmP arrivals from this region.

Within segment 28 (29–56 km model distance), layer 2A is slightly thicker at around 0.8 km, with more variable seabed velocities (2.4–4.1 km/s) and vertical velocity gradients (from 0.6/s to 1.7/s). Layer 2B has a roughly constant thickness of 1.9 km and velocities at its top are generally higher (up to 5.5 km/s) than in the NTD, with lower gradients. Here the mean thickness of layer 3 is 3.0 km, with a Moho depth of 8.6 km bsl. Beneath the NTD east of segment 28 (56–66 km model distance), layer 2B is slightly thicker (up to 2.4 km) with velocities at its top decreasing to 4.0–4.4 km/s, while layer 3 is a little thinner (at around 2.4 km).

Close to OBS 23 (at 70 km model distance), the Moho sharply deepens eastward (slope ∼20°) and the thickness of layer 3 increases dramatically. Within segment 27 (66–138 km in distance) both layer 2A and layer 2B have large variations in thickness (0.5–1.1and 0.9–1.5 km, respectively) but small lateral variations in velocity, and the velocity at the seabed reaches as low as 1.8 km/s. The thickness of layer 3 reaches 8.2 km and the maximum crustal thickness is 10.2 km. Although the Moho is deep within segment 27, PmP phases were observed with high amplitude on five instruments (OBS 23–30), providing strong constraints on Moho depth. Beneath the Moho, the velocity in upper mantle is 8.0 km/s throughout, constrained by Pn arrivals identified on record sections from OBS8, OBS4, OBS2, OBS11, OBS21, OBS23, and OBS24 (Figures 3–7).

4.3. Error Analysis and Uncertainty

Pick uncertainties and the travel time misfit of our best model are given in Table 1. Since the signal-noise ratio tends to decrease with increasing offset [*Zelt and Smith*, 1992; *Zelt and Forsyth*, 1994], we assigned

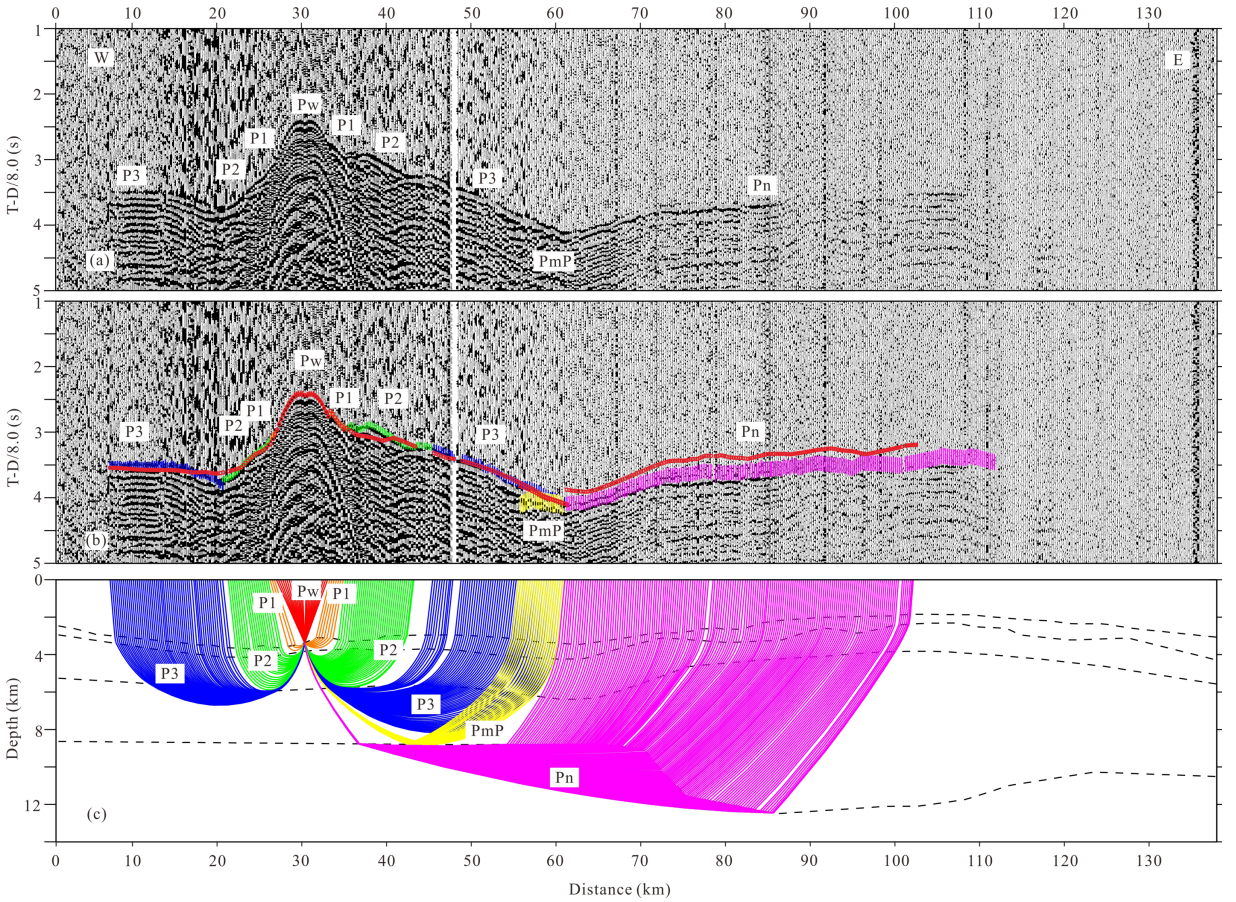

Figure 6. (a) A record section of the vertical component of OBS 4 on profile AB, (b) the record section with picked and calculated travel time overlain, and (c) ray diagram. The uncertainty of Pn increases with offset from 100 ms to 120 ms. Of 198 Pn picks, 80% are fitted with an RMS misfit of 221 ms and a χ^2 of 3.376.

uncertainties that varied with offset, and different phases were assigned different uncertainty ranges (Table 1). The overall root-mean-square (RMS) misfit was 103 ms, and misfit increased slightly with depth and offset. The overall χ^2 value was 1.347, with 94% of picks fitted, and the normalized travel time misfit suggests that the model was suitably parameterized, with a travel time misfit slightly larger than the pick uncertainty. The resolution of velocity nodes [*Zelt and Smith*, 1992] is shown in Figure 8 with black squares, with values greater than 0.5 considered to be well resolved and reliable. No values are shown in oceanic layer 3 or the mantle because here no lateral velocity variation was required to fit the data. There is a relationship between velocity uncertainty and resolution [*Zelt and Smith*, 1992], and we calculated the resolution using a velocity uncertainty of 0.2 km/s. The resolution of most velocity nodes in layer 2B is greater than 0.5. Some nodes in layer 2A have lower values because the velocity uncertainty of layer 2A is larger than 0.2 km/s (Table 2). The number of rays through each cell (0.5 km horizontally by 0.2 km in depth) was generally larger than 5 and reached over 100 (Figure 9), further indicating that the model is well constrained. We estimated uncertainties by using the *F* test to determine the size of perturbation required to give a statistically different misfit (Table 2) [*Zelt and Smith*, 1992; *Muller et al*., 1997]. These tests indicated that uncertainties in crustal velocities are less than 0.4 km/s and the uncertainty of Moho depth is $\pm$0.5 km

4.4. Gravity Modeling and Results

There are large differences between our seismically derived crustal thickness and the crustal thickness previously derived using gravity data [*Mendel et al*., 2003; *Sauter et al*., 2004] (Figure 10a). Therefore, we tested whether our model is consistent with gravity data. We used satellite-derived gravity anomaly data from a global 1 min gravity grid (version 18.1) [*Sandwell and Smith*, 2009]. We converted our velocity models to density models using the empirical velocity-density relationship for oceanic crust of *Carlson and Herrick* [1990]. The resulting density models consisted of constant-density polygons with corners corresponding to

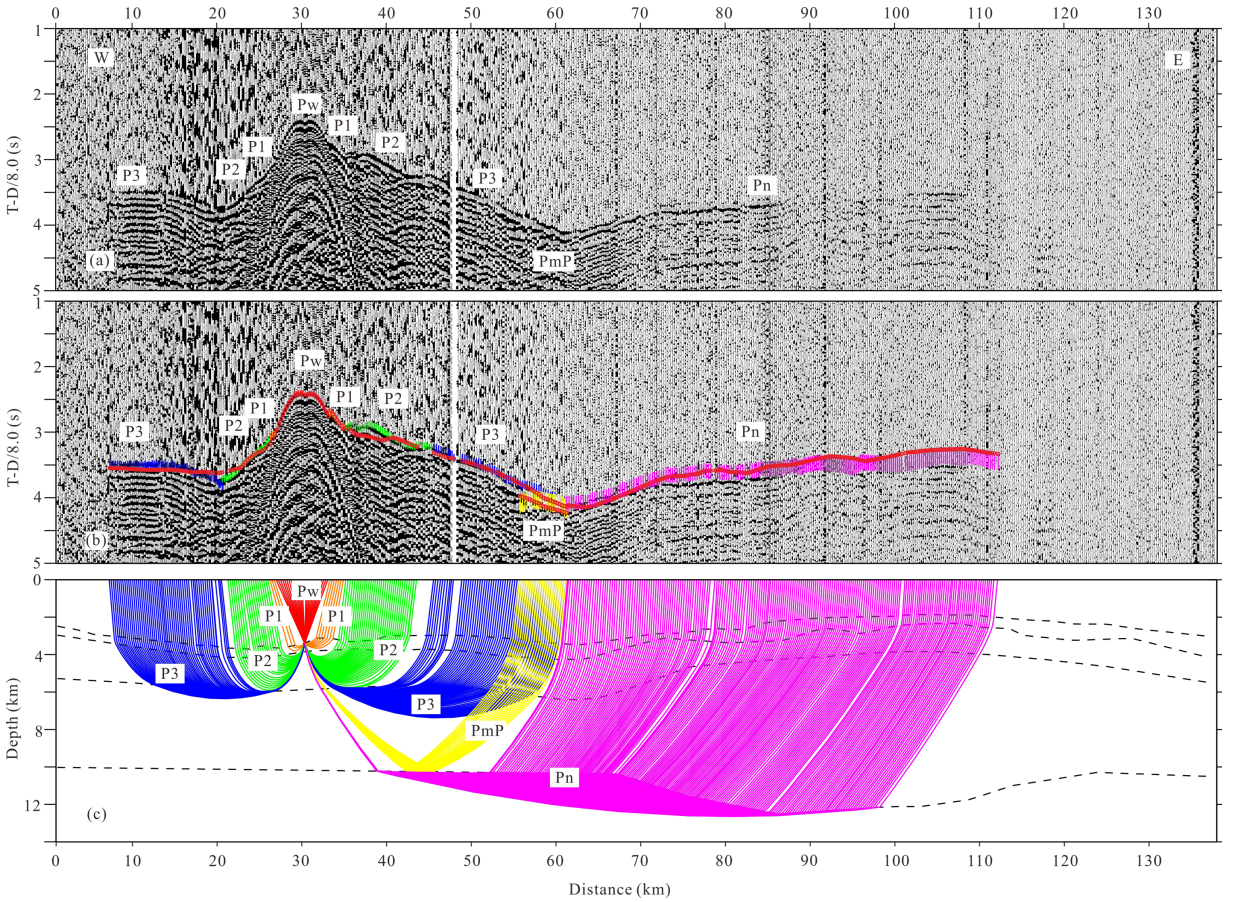

Figure 7. Alternative model with a deeper Moho at the western end. (a) A record section of the vertical component of OBS 4 on profile AB, (b) the record section with picked and calculated travel time overlain, and (c) ray diagram. Of 198 Pn picks, 100% are fitted with an RMS misfit of 86 ms and a χ^2 of 0.523.

seismic velocity nodes and mean densities derived from the mean seismic velocity within these polygons. Constant densities of 1025 and 3300 kg/m^3 were used for seawater and the mantle, respectively. Gravity anomalies were calculated using the method of *Talwani et al*. [1959]. The resulting mean crustal density (Figure 10b) shows density variations along the profile, from ~2650 kg m^{-3} at NTDs to ~2850 kg m^{-3} at segment centers. The calculated and observed gravity match well (Figure 10c), except at the ends of the profile, where the observed gravity may be influenced by unknown structures beyond the ends of the profile. Elsewhere the misfit rarely exceeds 10 mGal, and can be attributed to unmodeled three-dimensional effects. The key difference between our new gravity model and previously published gravity models is the inclusion of along-axis variations in crustal density, which can be significant at slow spreading mid-ocean ridges [*Minshull*, 1996]. The gravity fit for our preferred model is significantly better than that for the alternative model of Figure 7 (Figure 10c).

Table 1. Statistics of Travel Time Analysis[a]

Phase	Pw	P1	P2	P3	PmP	Pn	Total
Number of picks	316	56	544	1434	660	770	3780
Uncertainty (ms)[a]	30	50	50	62–73	119–164	100–188	89
RMS misfit (ms)	22	59	70	80	118	153	103
χ^2	0.525	1.433	1.948	1.454	0.713	1.479	1.347
Proportion of picks used (%)	98	86	88	97	99	90	94

[a]The main uncertainty is the picking uncertainty; other uncertainties come from uncertainties in OBS depth and position and total ~20 ms.

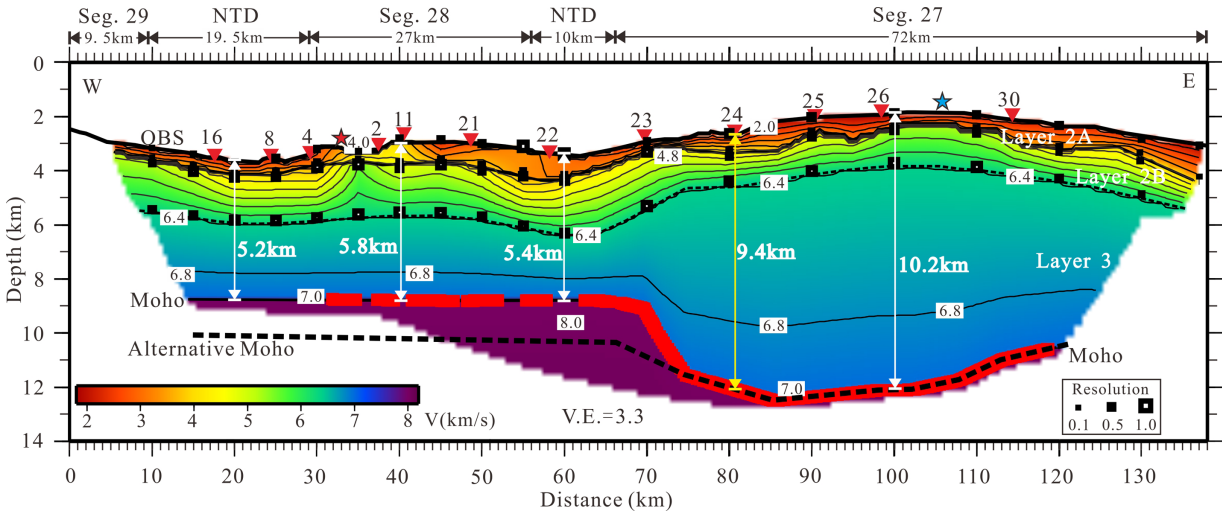

Figure 8. The final velocity model for profile AB. Numbered red triangles represent the OBS stations. Thin black lines represent the velocity contours every 0.4 km/s. Solid black lines represent the seabed and the Moho discontinuity. The red colored portion of the Moho marks sections constrained by PmP reflections. The thin dashed black line represents the interface between oceanic layers 2 and 3. The thick dashed black line represents the alternative Moho discontinuity of Figure 7. The black rectangles along the interfaces represent the resolution values for the velocity nodes, with a value of greater than 0.5 considered reliable [*Zelt and Smith*, 1992]. Values are plotted only within oceanic layer 2 because the deeper layers have no lateral velocity variations. The red and blue stars represent active and inactive hydrothermal vents, respectively. The 1D velocity of the white lines with arrows was shown in Figure 12.

We also calculated the load anomaly (Figure 10d) to test local isostasy situation along the seismic profile. The calculated load anomaly is intermediate between two end-member models: an Airy isostatic model with no load anomaly and a model with no compensation at all, in which the Moho is horizontal and the density of the crust varies as in Figure 10b. Therefore, we infer that there is only partial isostatic compensation and the axial lithosphere retains some flexural strength.

4.5. Comparison With Former Study

At 0–86 km model distance, our model traverses the 3-D model of *Zhao et al.* [2013]. The two models match well in oceanic layer 2 (Figure 11), though the 3-D model resolves some short-wavelength variations that are not resolved in our 2-D model. There are three main reasons for differences between the models: (1) differences in accuracy and resolution of the predefined seabed interface; (2) differences in data used and modeling approach; and (3) the effects of "out of plane" or 3-D ray sampling are ignored in the 2-D model [*Zelt and Zelt*, 1998]. The main difference between the models is in oceanic layer 3, where the 3-D model shows a region of reduced velocities in the segment center and higher velocities toward the segment ends. Our 2-D model does not resolve these velocity variations and throughout has velocities close to those of the segment center in the 3-D model. Because the 3-D model is based on first arrivals and has no velocity discontinuities, ray coverage in layer 3 is limited and layer 3 velocities potentially may be influenced by Pn arrivals. We attempted to develop a 2-D model with layer 3 velocities similar to those of the 3-D model, whilst retaining the Moho boundary of our 2-D model, but were unable to find one with an adequate travel time fit.

Table 2. Estimated Uncertainties of the Final Model Parameters

Model Parameter	Uncertainty
Top velocity of layer 2A	±0.3 km/s
Bottom velocity of layer 2A	±0.4 km/s
Top velocity of layer 2B	±0.2 km/s
Bottom velocity of layer 2B	±0.2 km/s
Top velocity of layer 3	±0.2 km/s
Bottom velocity of layer 3	±0.15 km/s
Top velocity of upper mantle	±0.2 km/s
Interface between layers 2A and 2B	±0.05 km
Interface between layers 2 and 3	±0.3 km
Moho discontinuity	±0.5 km

5. Discussion

5.1. Variable Velocity and Thickness in Layer 2A

It is widely accepted that oceanic layer 2A has low seismic velocities that rise rapidly with age, and that it remains a distinct layer even after 30–40 million years [e.g., *Carlson*, 1998]. It is interpreted to consist mainly of basaltic pillow lavas [e.g., *Christeson et al.*, 2007; *Spudich and Orcutt*, 1980], though more recent studies have emphasized the role of

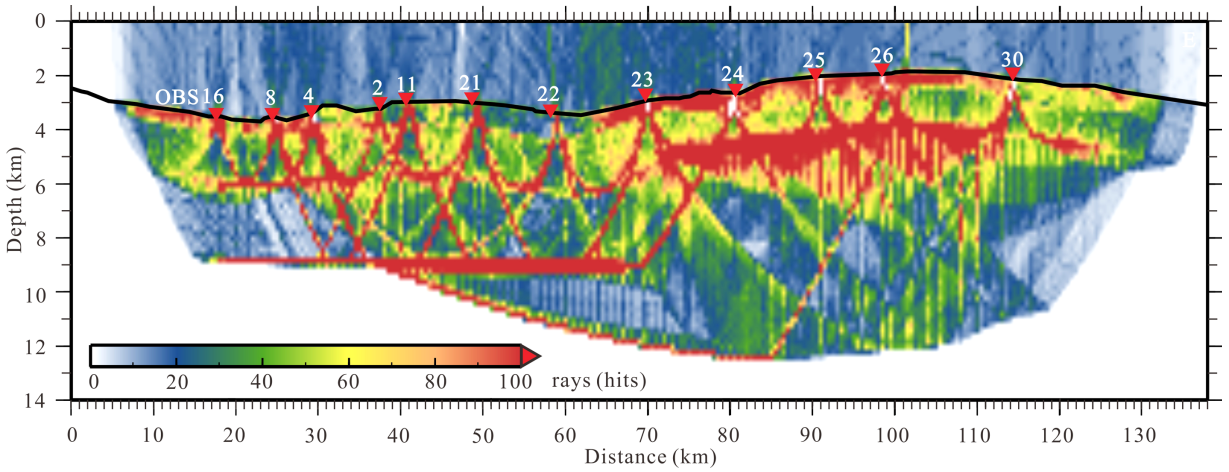

Figure 9. Ray density for 0.5 × 0.2 km cells. The seabed and OBS locations are marked as in Figure 8.

porosity rather than lithology in defining the layering [e.g., *Seher et al*., 2010; *Nedimović et al*., 2008].

Layer 2A in this study has variable thickness and velocity. The refracted phase P1 was not picked at every OBS because the layer is thin and P1 is often hidden by the water wave. Lateral variations in layer 2A velocity in segment 28 may arise mainly because the profile lies partly on the ridge axis (Figure 2), where it samples zero-age crust with velocity lower than 3 km/s [*Carlson*, 1998], and partly off the axis where velocities are larger. Deeper rocks may be exhumed by the detachment fault nearby [*Zhao et al*., 2013]. In segment 27, the profile is located on the ridge axis (Figure 2), and hence the layer 2A velocity is consistently low.

The variable layer 2A thickness of 0.5–1.1 km that we observe matches poorly the published relationship between the axial thickness of layer 2A and spreading rate [*Carbotte and Scheirer*, 2004; *Seher et al*., 2010]. Our range of observed thicknesses is more typical of intermediate spreading ridges—for example, the Valu Fa Ridge, where the thickness varies between 0.4 and 1.0 km [*Day et al*., 2001; *Jacobs et al*., 2007]. Because the layer 2A thickness is constrained by the first emergence of phase P2 from the layer beneath, its uncertainty is small—around 50 m. A possible explanation for the observed thickness of layer 2A is that the SWIR at 50°E has an enhanced melt supply [*Sauter et al*., 2001, 2004; *Tao et al*., 2009] and therefore more vigorous extrusive magmatism than typical at ultraslow spreading rates.

5.2. Differences of Layer 2B Between NTDs and Segment Centers

Layer 2B is characterized seismically by *P* wave velocities of 5.2 ± 0.4 km/s at the top to 6.4 km/s at the base [*Carlson*, 1998], and a steep velocity gradient (∼1–2/s) [*Spudich and Orcutt*, 1980], and is interpreted primarily as sheeted dykes [e.g., *Wilson et al*., 2006; *Newman et al*., 2011]. The same characteristics can be found in our velocity model (Figure 8). While in the previous more coarsely sampled study of the SWIR axis, the main difference between segment centers and NTDs occurred in layer 3 and little difference was detected in layer 2 [e.g., *Minshull et al*., 2006], our study shows a clear difference in layer 2B velocity between segment centers and NTDs (Figure 8). Both NTDs in velocity model show a lower velocity at the top of layer 2B (4.0 km/s) than at the segment centers (4.8 km/s). We infer that tectonic processes dominate in the NTDs, with more fractures generated [*White et al*., 2001] and deeper penetration of seawater [*Sauter et al*., 2004].

5.3. The Implications of Thick Crust Beneath Segment 27

We compared velocity-depth profiles at model distances of 20 km (NTD), 40 km (segment 28 center), 60 km (NTD), and 100 km (segment 27 center) with velocity-depth profiles at other ridges with similar spreading rates and with 0.7 Ma crust at the Mid-Atlantic Ridge (Figure 12). Layer 2 velocity structures vary little between these profiles, though parts of the Gakkel Ridge have much lower velocities. There is much greater variation in layer 3, where segment 27 shows unusually low velocities and thick crust.

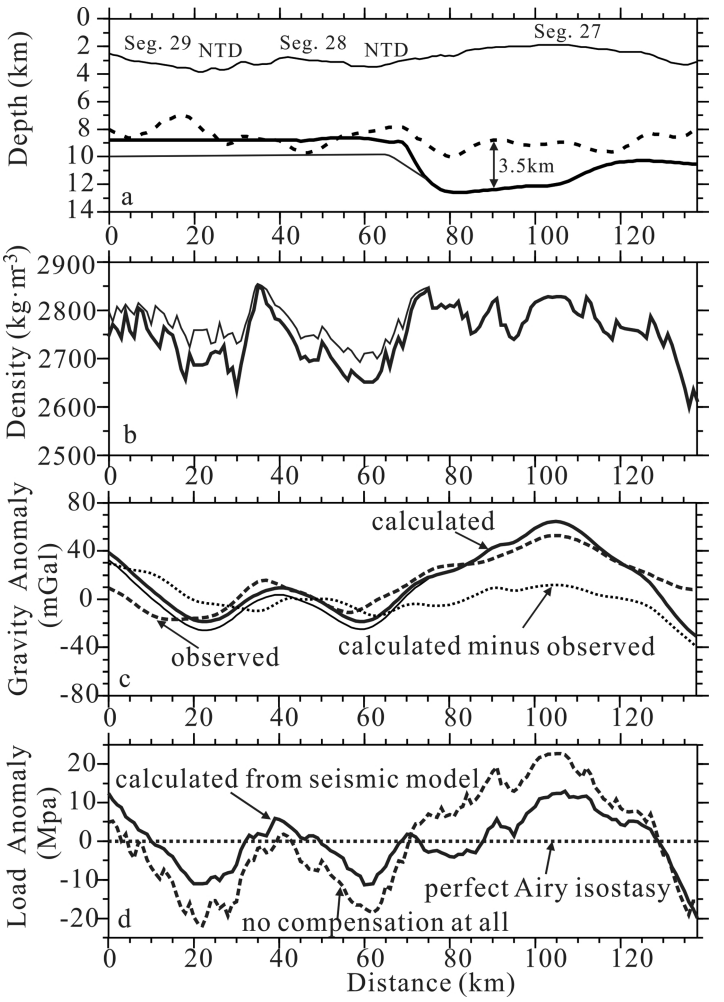

Figure 10. (a) Comparison of Moho depth variations determined from our seismic profile (thick solid line) with the Moho depth determined along the same profiles by *Sauter et al.* [2004] using gravity data (dashed line). The thin solid line is seabed. The Moho depth from gravity modelling in Segment 27 is up to 3.5 km shallower than the seismic Moho (see explanation in the text). (b) Mean crustal density along the profile. The density values are calculated by using a velocity and density relationship of ρ=3.81−6.0/*Vp* [*Carlson and Herrick*, 1990]. (c) Dashed line marks satellite-derived gravity anomaly. Thick solid line marks the gravity anomaly calculated for a model in which our preferred seismic velocity model is converted to density. Thinner solid line marks the calculated anomaly corresponding to the alternative seismic velocity model of Figure 8. Dotted line marks the residual for our preferred model (calculated minus observed). (d) Load anomaly corresponding to our preferred density model. The no compensation curve is calculated with a water density of 1025 kg/m^3, constant crust density as shown in Figure 10b, a mantle density of 3300 kg/m^3, and a horizontal Moho at the mean seismically determined Moho depth of 10.55 km.

Sauter et al. [2009] inferred the presence of regionally thicker crust (Figure 10a) since ~10 Ma between the Indomed and Gallieni TFs relative to the neighboring ridge sections from an analysis of off-axis bathymetry and gravity data. A low magnetization anomaly at the center of segment 27 also suggests that the magmatic activity is high enough to limit lava fractionation there [*Sauter et al.*, 2004]. In addition, the lower Na_8 contents of basalts in this region indicate higher melt production than beneath the neighboring deeper ridge sections [*Cannat et al.*, 2008]. Other geochemical proxies, such as $(Sm/Yb)_n$ or CaO/Al_2O_3, also support a larger magma budget in the subaxial mantle of this ridge region [*Meyzen et al.*, 2003].

The regionally thicker crust in the central shallow part of the SWIR may be explained either by increased mantle temperature [*Cannat et al.*, 2008] or by increased mantle fertility [*Zhou and Dick*, 2013]. Large negative anomalies of *S* wave velocities, which are particularly sensitive to temperature, have been identified at 75 km depth beneath the shallow central part of the SWIR in the global tomographic model of *Debayle et al.* [2005]. Using a one-dimensional mantle melting model *Cannat et al.* [2008] showed that a change of about 60°C in the temperature of the subaxial mantle from the central shallow part to the easternmost part of the SWIR, consistently with the broad geoid high observed over the same area, can explain the along-axis large-scale variation of the ridge's melt supply. A recent geochemical study on the Crozet hot spot suggests that the shallow mantle between the Indomed and Gallieni TFs may be contaminated by deep material from the Crozet plume [*Breton et al.*, 2013]. A flow of plume-derived mantle material to the ridge and down the subaxial asthenospheric channel can result in increased mantle temperature, ridge topography, and crustal thickness [*Morgan*, 1972]. However, the Crozet archipelago is more than 1000 km far away from the ridge axis, much further than the distance of 500 km beyond which the influence of a hot spot is thought to become less significant [*Ito and Lin*, 1995; *Ribe et al.*, 1995; *Ito et al.*, 2003].

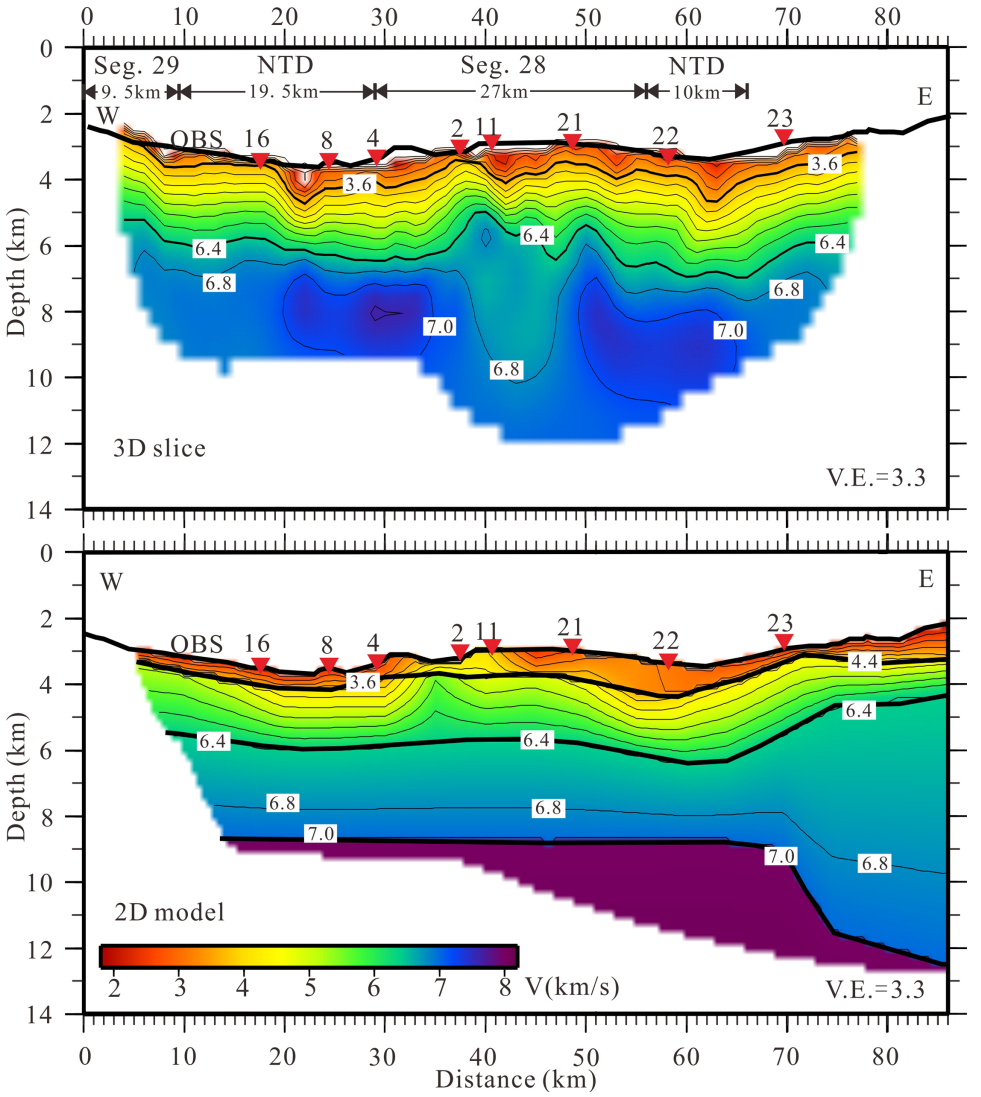

Figure 11. A comparison with the 3D model of *Zhao et al.* [2013]. The upper panel shows the 3D model sampled along our 2D profile, with white regions just below the seabed marking areas where the velocities recovered were unacceptably low (~1.5 km/s). The lower panel shows the corresponding part of our 2D model.

Because peridotites are exposed over the shallow central part of the SWIR *Zhou and Dick* [2013] argue that the average crustal thickness could be about 2 km which, they proposed, is not enough to explain the formation of the central shallow part of the SWIR using any thermal model that precludes mantle compositional buoyancy as the major contributor. These authors suggest that the density contrast between fertile garnet lherzolite and depleted harzburgite can account for the depth variation along the SWIR [*Zhou and Dick*, 2013]. Although we have shown that the crust is much thicker than the estimate of *Zhou and Dick* [2013], we note that the melting of more fertile mantle heterogeneities can indeed explain areas of locally thicker crust (>8 km) such as at the Mid-Atlantic Ridge at 33°S [*Michael et al.*, 1994], 8°S–9°S [*Minshull et al.*, 1998b, 2003], or 33°S–35°S [*Niu et al.*, 2001]. The melting of such mantle heterogeneity could have resulted, ~8–11 Ma ago, in the formation of the shallow domain between Indomed and Gallieni TF culminating at the magmatically robust segment 27. We have shown that the local depth anomaly associated with this segment is partly sustained by the finite strength of the axial lithosphere. However, the crust older than 11 Ma is deeper and thinner [*Sauter et al.*, 2009] indicating that a region of previously depleted mantle, as proposed by *Zhou and Dick* [2013], may have supported the much weaker regional depth anomaly at that time.

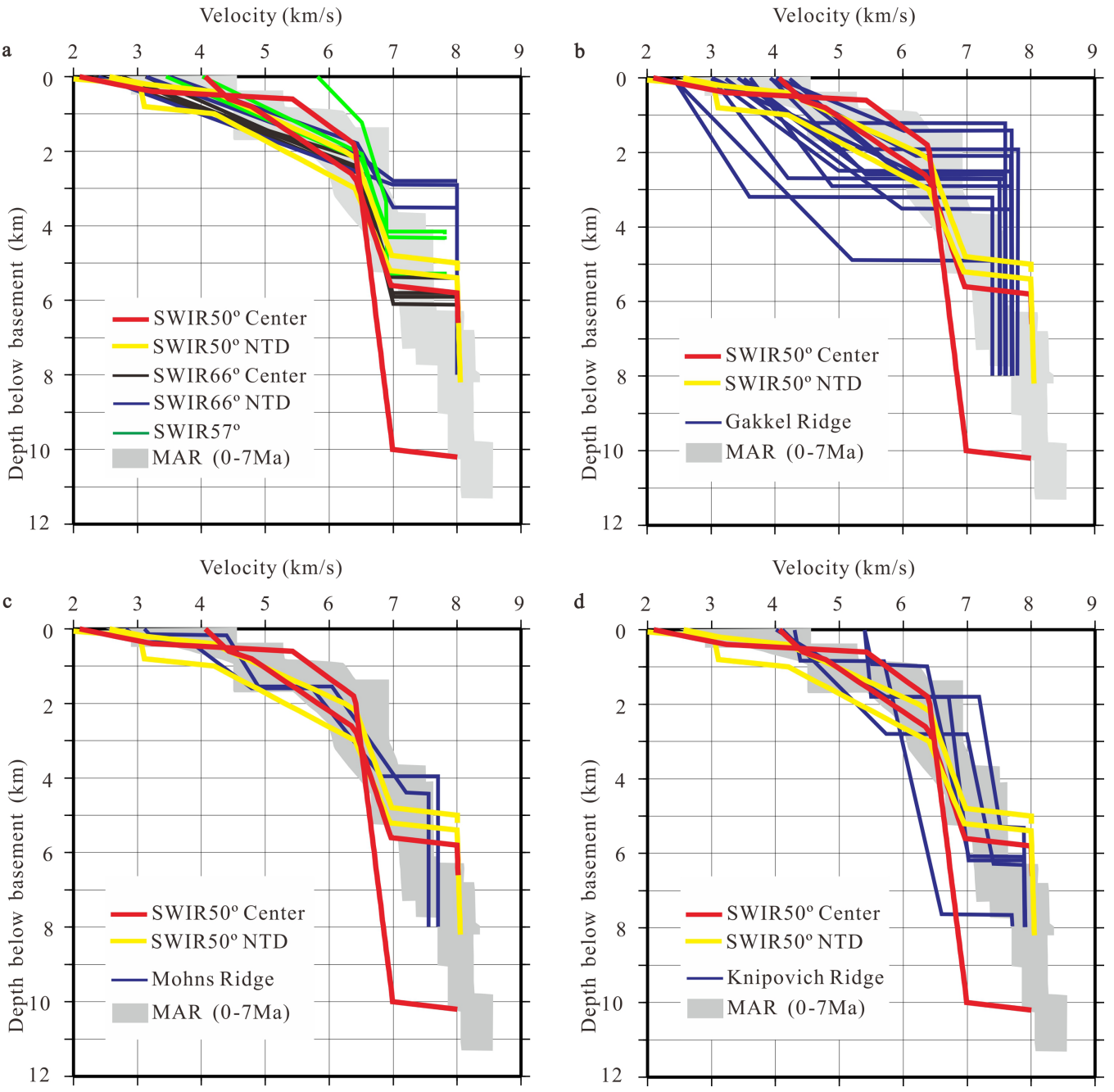

Figure 12. Comparison of velocity-depth variations sampled from our preferred model (yellow and red) with those determined elsewhere at ultra-slow spreading ridges. (a) SWIR at 57°E [*Muller et al.*, 2000] and 66°E [*Minshull et al.*, 2006]; (b) Gakkel Ridge [*Jokat and Schmidt-Aursch*, 2007]; (c) Mohns Ridge [*Klingelhofer et al.*, 2000]; (d) Knipovich Ridge [*Kandilarov et al.*, 2010]. The shaded envelope bounds velocities for 0-7 Ma Atlantic crust from *White et al.* [1992].

Finally, whatever the origin of the thick crust area at the SWIR, we emphasize that our observation of thick crust at an ultraslow spreading ridge complicates the variation of crustal thickness with spreading rate and associated models [*White et al.*, 2001; *Cannat et al.*, 2008; *Sauter and Cannat*, 2010; *Sauter et al.*, 2011]. It supports previous suggestions that the extent of mantle melting is not a simple function of spreading rate and that mantle temperatures or mantle chemistry (or both) must vary significantly along axis [e.g., *Michael et al.*, 2003].

5.4. Small NTD Between SWIR Segments 28 and 27

The crust at the NTD between segments 28 and 27 is ~2 km thicker than crust at NTDs at 66°E [*Minshull et al*., 2006] (Figure 12a). This difference can be explained by a model of magma supply [*Sauter et al*., 2001], in which thin crust and reduced volcanic production occur at discontinuities with offsets larger than 15 km, but there is little or no volcanic production or crustal thickness variation associated with smaller NTDs. The NTD between segments 28 and 27 is 10 km in length [*Sauter et al*., 2004], while at 66°E the NTDs are larger [*Minshull et al*., 2006; *Sauter et al*., 2004]. Therefore, the melt production at 50°E is not as focused as at 66°E. The NTD west of segment 28 is larger, but here constraints on crustal thickness are weaker.

5.5. Crust Thickness Varies Between Segments 28 and 27

The thickness of oceanic layer 3 varies greatly (between 2.5 and 8.0 km) along the profile, consistent with previous observations that crustal thickness variations occur primarily in layer 3 [*Minshull et al*., 2006]. However, the ~5 km thickness difference between two neighboring segment centers is still remarkable. We attribute the difference to focusing of melt delivery in the crust [*White et al*., 2001], though the NTD between the two segments is small, so the precise mechanism remains poorly understood.

5.6. Unaltered Mantle

Another important difference from ultraslow spreading ridges elsewhere is our observed velocity of 8.0 ± 0.2 km/s in the uppermost mantle. Uppermost mantle velocities are 7.4–7.7 km/s at the Gakkel Ridge [*Jokat and Schmidt-Aursch*, 2007], 7.5–7.7 km/s at the Mohns Ridge [*Klingelhöfer et al*., 2000] and 7.6–7.9 km/s at the Knipovich Ridge [*Kandilarov et al*., 2010] (Figure 12). For normal oceanic lithosphere, the *P* wave velocity immediately beneath the oceanic Moho is typically 7.9–8.3 km/s [*White et al*., 2001]. Reduced upper mantle velocities at other ultraslow ridges may result from serpentinization [e.g., *Klingelhöfer et al*., 2000], which appears to be limited to ~5 km depth in the oceanic crust [*Minshull et al*., 1998a], and therefore may be absent beneath the thicker crust that we observe. Alternatively, velocities may be reduced by the presence of trapped melt in the uppermost mantle [*Cannat*, 1996; *Lizzaralde* et al., 2004]. The normal mantle velocities inferred from our seismic data suggest that neither serpentinization nor freezing of melt in the mantle are important processes beneath the SWIR at 50°E.

6. Conclusions

From our study of the seismic crustal structure of the SWIR at 50°E, we draw the following conclusions:

1. Oceanic layers 2A, 2B, and 3 are present. Layer 2A varies in velocity and thickness along the profile. Layer 2B has a steep velocity gradient, and varies little in thickness in segment 28 and at NTDs, but has greater thickness variation in segment 27. Our data require no lateral velocity variation in layer 3 but the layer 3 thickness varies significantly between segments 27 and 28.

2. Variations in layer 2A velocity may be explained largely by variations in crustal age along the profile. The layer 2A thickness is more typical of an intermediate spreading ridge than an ultraslow spreading ridge, suggesting that this thickness is strongly influenced by melt supply.

3. Reduced velocities at the top of layer 2B in the NTDs may be explained by increased tectonic extension in these regions.

4. Crustal thickness reaches 10.2 km beneath the center of segment 27 (50°28′E), suggesting that there is a hot mantle and/or fertile melt beneath it.

5. The melt supply to the ridge axis is focused toward segment centers, despite the relatively short NTD between them.

6. Beneath the thick crust we observe normal upper mantle velocities (8.0 ± 0.2km/s), suggesting that there is insufficient penetration of seawater to cause significant mantle serpentinization, and that no significant volume of melt has been trapped in the mantle.

Acknowledgments
We are grateful to the scientists and crew of DY115-21 cruise (Leg 6) of the R/V "DayangYihao." The seismic experiment and our research are supported by the National Basic Research program of China (grant 2012CB417301) and the National Natural Science Foundation of China (grants 41176046, 41176053, and 91228205). We used the RayInvr code [*Zelt and Smith*, 1992] for seismic inversion. Some of our figures were plotted using GMT [*Wessel and Smith*, 1995]. Data analysis was completed during a visit by X.N. to the National Oceanography Centre Southampton, University of Southampton. We thank Xiaodong Wei, Tao Zhang, Zhaocai Wu, Haibo Huang, and Junjiang Zhu for discussions and Frauke Klingelhoefer and Bob White for detailed and constructive reviews.

References

Ao, W., M. H. Zhao, X. L. Qiu, J. B. Li, A. G. Ruan, S. J. Li, and J. Z. Zhang (2010), The correction of shot and OBS position in the 3D seismic experiment of the SW Indian Ocean Ridge [in Chinese], *Chin. J. Geophys.*, *53*(6), 1072–1081, doi:10.3969/j.issn.0001–5733.2010.12.022.

Bown, J. W., and R. S. White (1994), Variation with spreading rate of oceanic crustal thickness and geochemistry, *Earth Planet. Sci. Lett.*, *121*, 435–449, doi:10.1016/0012-821X(94)90082-5.

Breton, T., F. Nauret, S. Pichat, B. Moine, M. Moreira, E. F. Rose-Koga, D. Auclair, C. Bosq, and L. Wavrant (2013), Geochemical heterogeneities within the Crozet hotspot, *Earth Planet. Sci. Lett.*, *376*, 126–136, doi:10.1016/j.epsl.2013.06.020.

Cannat, M. (1996), How thick is the magmatic crust at slow-spreading oceanic ridges?, *J. Geophys. Res.*, *101*, 2847–2857, doi:10.1029/95JB03116.

Cannat, M., C. Rommevaux-Jestin, D. Sauter, C. Deplus, and V. Mendel (1999), Formation of the axial relief at the very slow spreading Southwest Indian Ridge (49° to 69°E), *J. Geophys. Res.*, *104*, 2825–2843, doi:10.1029/1999JB900195.

Cannat, M., D. Sauter, V. Mendel, E. Ruellan, K. Okino, J. Escartin, V. Combier, and M. Baala (2006), Modes of seafloor generation at a melt-poor ultra-slow-spreading ridge, *Geology*, *34*(7), 605–608, doi:10.1130/G22486.1.

Cannat, M., D. Sauter, A. Bezos, C. Meyzen, E. Humler, and M. Le Rigoleur (2008), Spreading rate, spreading obliquity, and melt supply at the ultraslow spreading Southwest Indian Ridge, *Geochem. Geophys. Geosyst.*, *9*, Q04002, doi:10.1029/2007GC001676.

Carbotte, S., and D. Scheirer (2004), Variability of ocean crustal structure created along the global mid-ocean ridge, in *Hydrogeology of the Oceanic Lithosphere*, edited by E. E. Davis and H. Elderfield, pp. 59–107, Cambridge Univ. Press, Cambridge, U. K.

Carlson, R. L. (1998), Seismic velocities in the uppermost oceanic crust: Age dependence and the fate of layer 2A, *J. Geophys. Res.*, *103*, 7069–7077, doi:10.1029/97JB03577.

Carlson, R. L. and C. N. Herrick (1990), Densities and porosities in the oceanic crust and their variations with depth and age, *J. Geophys. Res.*, *95*, 9153–9170, doi:10.1029/JB095iB06p09153.

Christeson, G. L., K. D. McIntosh, and J. A. Karson (2007), In consistent correlation of seismic Layer2a and lava layer thickness in oceanic crust, *Nature*, *445*, 418–421, doi:10.1038/nature05517.

Chu, D., and R. G. Gordon (1999), Evidence for motion between Nubia and Somalia 587 along the Southwest Indian Ridge, *Nature*, *398*, 64–67, doi:10.1038/18014.

Curray, J. R., and T. Munasinghe (1991), Origin of the Rajmahal Traps and the 85°E Ridge: Preliminary reconstructions of the trace of the Crozet hotspot, *Geology*, *19*, 1237–1240, doi:10.1130/0091-7613(1991).

Day, A., C. Peirce, and M. Sinha (2001), Three dimensional crustal structure and magma chamber geometry at the intermediate spreading, back arc Valu Fa Ridge, Lau Basin—Results of a wide angle seismic tomographic inversion, *Geophys. J. Int.*, *146*, 31–52, doi:10.1046/j.0956-540x.2001.01446.x.

Debayle, E., B. Kennett and K. Priestley (2005), Global azimuthal seismic anisotropy and the unique plate-motion deformation of Australia, *Nature*, *433*, 509–512, doi:10.1038/nature03247.

Dick, H. J. B., J. Lin, and H. Schouten (2003), An ultraslow-spreading class of ocean ridge, *Nature*, *426*, 405–412, doi:10.1038/nature02128.

Georgen, J. E., J. Lin, and H. J. B. Dick (2001), Evidence from gravity anomalies for interactions of the Marion and Bouvet hotspots with the Southwest Indian Ridge: Effects of transform offsets, *Earth Planet. Sci. Lett.*, *187*, 283–300, doi:10.1016/S0012-821X (01)00293-X.

Goslin, J., and M. Diament (1987), Mechanical and thermal isostatic response of the Del Cano Rise and Crozet Bank (southern Indian Ocean) from altimetry data, *Earth Planet. Sci. Lett.*, *84*, 285–294, doi:10.1016/0012-821X (87)90093-8.

Ito, G., and J. Lin (1995), Oceanic spreading center-hotspot interactions: Constraints from along-isochron bathymetry and gravity anomalies, *Geology*, *23*, 657–660, doi:10.1130/0091-7613(1995)023<0657:OSCHIC>2.3.CO;2.

Ito, G., J. Lin, and D. W. Graham (2003), Observational and theoretical studies of the dynamics of mantle plume-mid-ocean ridge interaction, *Rev. Geophys.*, *41*(4), 1017, doi:10.1029/2002RG000117.

Jacobs, A. M., A. Harding, and G. Kent (2007), Axial crustal structure of the Lau back arc basin from velocity modeling of multichannel seismic data, *Earth Planet. Sci. Lett.*, *259*, 239–255, doi:10.1016/j.epsl.2007.04.021.

Jokat, W., and M. C. Schmidt-Aursch (2007), Geophysical characteristics of the ultraslow spreading Gakkel Ridge, Arctic Ocean, *Geophys. J. Int.*, *168*(3), 983–998, doi:10.1111/j.1365-246X.2006.03278.x.

Kandilarov, A., H. Landa, R. Mjelde, R. B. Pedersen, K. Okino, and Y. Murai (2010), Crustal structure of the ultra-slow spreading Knipovich Ridge, North Atlantic, along a presumed ridge segment center, *Mar. Geophys. Res.*, *31*(3), 173–195, doi:10.1007/s11011-010-9095-8.

Kennett, J. P. (1982), *Marine Geology*, 813 pp., Prentice Hall, Englewood Cliffs, N. J.

Klingelhöfer, F., L. Géli, L. Matias, N. Steinsland, and J. Mohr (2000), Crustal structure of a super-slow spreading centre: A seismic refraction study of the Mohns Ridge, 72°N, *Geophys. J. Int.*, *141*(2), 509–526, doi:10.1046/j.1365-246x.2000.00098.x.

Li, J. B., and Y. J. Chen (2010), First Chinese OBS experiment at Southwest Indian Ridge, *InterRidge News*, *19*, 16–28.

Lizzaralde, D., J. B. Gaherty, J. A. Collins, G. Hirth, and S. D. Kim (2004), Spreading-rate dependence of melt extraction at mid-ocean ridges from mantle seismic refraction data, *Nature*, *432*, 744–747, doi:10.1038/nature03140.

Mahoney, J. J., W. M. White, B. G. J. Upton, C. R. Neal, and R. A. Scrutton (1996), Beyond EM-1: Lavas from Afanasy-Nikitin Rise and the Crozet Archipelago, Indian Ocean, *Geology*, *24*, 615–618, doi:10.1130/0091-7613.

Mendel, V., D. Sauter, C. Rommevaux-Jestin, P. Patriat, F. Lefebvre, and L. M. Parson (2003), Magmato-tectonic cyclicity at the ultra-slow spreading Southwest Indian Ridge: Evidence from variations of axial volcanic ridge morphology and abyssal hills pattern, *Geochem. Geophys. Geosyst.*, *4*(5), 9102, doi:10.1029/2002GC000417.

Meyzen, C. M., M. J. Toplis, E. Humler, J. N. Ludden, and C. Mével (2003), A discontinuity in mantle composition beneath the southwest Indian Ridge, *Nature*, *421*, 731–733, doi:10.1038/nature01424.

Michael, P. J., et al. (1994), Mantle control of a dynamically evolving spreading center: Mid-Atlantic Ridge 31–34°S, *Earth Planet. Sci. Lett.*, *121*, 451–468, doi:10.1016/0012-821X(94)90083-3.

Michael, P. J., C. H. Langmuir, H. J. B. Dick, J. Snow, S. Goldstein, D. Graham, K. Lehnert, G. Kurras, R. Mühe, and H. Edmonds (2003), Magmatic and amagmatic seafloor spreading at the slowest mid-ocean ridge: Gakkel Ridge, Arctic Ocean, *Nature*, *423*, 956–961, doi:10.1038/nature01704.

Minshull, T. A. (1996), Along-axis variations in oceanic crustal density and their contribution to gravity anomalies at slow-spreading ridges, *Geophys. Res. Lett.*, *23*, 849–852.

Minshull, T. A., M. R. Muller, C. J. Robinson, R. S. White, and M. J. Bickle (1998a), Is the oceanic Moho a serpentinisation front?, *Geol. Soc. Spec. Publ.*, *148*(1), 71–80, doi:10.1144/GSL.SP.1998.148.01.05.

Minshull, T. A., N. J. Bruguier, and J. M. Brozena (1998b), Ridge-plume interactions or mantle heterogeneity near Ascension Island?, *Geology*, *26*, 115–118, doi:10.1130/0091–7613(1998)026<0115:RPIOMH>2.3.CO;2.

Minshull, T. A., N. J. Bruguier, and J. M. Brozena (2003), Seismic structure of the Mid-Atlantic Ridge, 8–9°S, *J. Geophys. Res.*, *108*(B11), 2513, doi:10.1029/2002JB002360.

Minshull, T. A., M. R. Muller, and R. S. White (2006), Crustal structure of the Southwest Indian Ridge at 66°E: Seismic constraints, *Geophys. J. Int.*, *166*, 135–147, doi:10.1111/j.1365-246X.2006.03001.x.

Morgan, W. J. (1972), Deep mantle convection plumes and plate motions, *Am. Assoc. Pet. Geol. Bull.*, *56*, 203–213.

Muller, M. R., C. J. Robinson, T. A. Minshull, R. S. White, and M. J. Bickle (1997), Thin crust beneath Ocean Drilling Program borehole 735B at the Southwest Indian Ridge?, *Earth Planet. Sci. Lett.*, *148*, 93–107, doi:10.1016/S0012-821X (97)00030-7.

Muller, M. R., T. A. Minshull, and R. S. White (1999), Segmentation and melt supply on the Southwest Indian Ridge, *Geology*, *27*, 867–870, doi:10.1130/0091-7613(1999).

Muller, M. R., T. A. Minshull, and R. S. White (2000), Crustal structure of the South West Indian ridge at the Atlantis II Fracture Zone, *J. Geophys. Res.*, *105*, 25,809–25,828, doi:10.1029/2000JB900262.

Muller, R. D., J. Y. Royer, and L. A. Lawver (1993), Revised plate motions relative to the hotspots from combined Atlantic and Indian Ocean hotspot tracks, *Geology*, *21*, 275–278, doi:10.1130/0091-7613(1993).

Nedimović, M. R., S. M. Carbotte, J. B. Diebold, A. J. Harding, J. P. Canales, and G. M. Kent (2008), Upper crustal evolution across the Juan de Fuca ridge flanks, *Geochem. Geophys. Geosyst.*, *9*, Q09006, doi:10.1029/2008GC002085.

Newman, K. R., M. R. Nedimović, J. P. Canales, and S. M. Carbotte (2011), Evolution of seismic layer 2B across the Juan de Fuca Ridge from hydrophone streamer 2D traveltime tomography, *Geochem. Geophys. Geosyst.*, *12*, Q05009, doi:10.1029/2010GC003462.

Niu, Y., D. Bideau, D. Hékinian, and R. Batiza (2001), Mantle compositional control on the extent of mantle melting, crust production, gravity anomaly, ridge morphology, and ridge segmentation: A case study at the Mid-Atlantic Ridge 33–35°N, *Earth Planet. Sci. Lett.*, *186*, 383–399, doi:10.1016/S0012-821X (01)00255-2.

Raitt, R. (1963), The crustal rocks, *Sea*, *3*, 85–102.

Recq, M., J. Goslin, P. Charvis, and S. Pperto (1998), Small-scale crustal variability within an intraplate structure: The Crozet Bank (southern Indian Ocean), *Geophys. J. Int.*, *134*, 145–156, doi:10.1046/j.1365-246x.1998.00530.x.

Reid, I., and H. Jackson (1981), Oceanic spreading rate and crustal thickness, *Mar. Geophys. Res.*, *5*(2), 165–172.

Ribe, N., U. R. Christensen, and J. Theißing (1995), The dynamics of plumeridge interaction. 1: Ridge-centered plumes, *Earth Planet. Sci. Lett.*, *134*, 155–168.

Sandwell, D. T., and W. H. F. Smith (2009), Global marine gravity from retracked Geosat and ERS-1 altimetry: Ridge segmentation versus spreading rate, *J. Geophys. Res.*, *114*, B01411, doi:10.1029/2008JB006008.

Sauter, D., and M. Cannat (2010), The ultraslow spreading Southwest Indian Ridge diversity of hydrothermal systems on slow spreading ocean ridges, *Geophys. Monogr. Ser.*, *188*, 153–173, doi:10.1029/2008GM000843.

Sauter, D., P. Patriat, C. Rommevaux-Jestin, M. Cannat, A. Briais, and Gallieni Shipboard Scientific Party (2001), The Southwest Indian Ridge between 49°15′E and 57°E: Focused accretion and magma redistribution, *Earth Planet. Sci. Lett.*, *192*, 303–317, doi:10.1016/S0012-821X(01)00455-1.

Sauter, D., H. Carton, V. Mendel, M. Munschy, C. Rommevaux-Jestin, J. J. Schott, and H. Whitechurch (2004), Ridge segmentation and the magnetic structure of the Southwest Indian Ridge (at 55°30′E, 55°30′E and 66°20′E): Implications for magmatic processes at ultraslow-spreading centers, *Geochem. Geophys. Geosyst.*, *5*, Q05K08, doi:10.1029/2003GC000581.

Sauter, D., M. Cannat, C. Meyzen, A. Bezos, P. Patriat, E. Humler, and E. Debayle (2009), Propagation of a melting anomaly along the ultra-slow Southwest Indian Ridge between 46°E and 52°20′E: Interaction with the Crozet hotspot?, *Geophys. J. Int.*, *179*, 687–699, doi: 10.1111/j.1365-246X.2009.04308.x.

Sauter, D., H. Sloan, M. Cannat, J. Goff, P. Patriat, M. Schaming, and W. R. Roest (2011), From slow to ultra-slow: How does spreading rate affect seafloor roughness and crustal thickness?, *Geology*, *39*(10), 911–914, doi:10.1130/G32028.1.

Sauter, D., et al. (2013), Continuous exhumation of mantle-derived rocks at the Southwest Indian Ridge for 11million years, *Nat. Geosci.*, *6*, 314–320, doi:10.1038/ngeo1771.

Seher, T., W. C. Crawford, S. C. Singh, and M. Cannat (2010), Seismic layer 2A variations in the Lucky Strike segment at the Mid-Atlantic Ridge from reflection measurements, *J. Geophys. Res.*, *115*, B07107, doi:10.1029/2009JB006783.

Spudich, P., and J. Orcutt (1980), Petrology and porosity of an oceanic site: Results from wave form modeling of seismic refraction data, *J. Geophys. Res.*, *85*, 1409–1433.

Standish, J. J., H. J. B. Dick, P. J. Michael, W. G. Melson, and T. O'Hearn (2008), MORB generation beneath the ultraslowspreading Southwest Indian Ridge (9°–25°E): Major element chemistry and the importance of process versus source, *Geochem. Geophys. Geosyst.*, *9*, Q05004, doi:10.1029/2008GC001959.

Storey, M., J. J. Mahoney, A. D. Saunders, R. A. Duncan, S. P. Kelley, and M. F. Coffin (1995), Timing of hot spot-related volcanism and the breakup of Madagascar and India, *Science*, *267*, 852–855, doi:10.1126/science.267.5199.852.

Talwani, M., J. L. Worzel, and M. Landisman (1959), Rapid gravity computations for two-dimensional bodies with application to the Mendocino submarine fracture zone, *J. Geophys. Res.*, *64*, 49–59.

Tao, C., et al. (2009), New hydrothermal fields found along the Southwest Indian Ridge during the Legs 5–7 Chinese DY115-20 expedition, *Eos Trans. AGU*, *90*(52), Fall Meet. Suppl., Abstract OS21A-1150.

Tao, C., H. Li, W. Huang, X. Han, G. Wu, X. Su, N. Zhou, J. Lin, Y. He, and J. Zhou (2011), Mineralogical and geochemical features of sulfide chimney from the 49°39′E hydrothermal field on the Southwest Indian Ridge and their geological significance, *Chin. Sci. Bull.*, *56*, 2828–2838, doi:10.1007/s11434-011-4619-4.

Tao, C., et al. (2012), First active hydrothermal vents on an ultraslow-spreading center: Southwest Indian Ridge, *Geology*, *40*, 47–50, doi: 10.1130/G32389.1.

Wessel, P., and W. H. F. Smith (1995), New version of Generic Mapping Tools released, *Eos Trans. AGU*, *76*(29), 329.

White, R. S., D. McKenzie, and R. K. ÓNions (1992), Oceanic crustal thickness from seismic measurements and rare earth element inversions, *J. Geophys. Res.*, *97*, 19,683–19,715, doi:10.1029/92JB01749.

White, R. S., T. A. Minshull, M. Bickle, and C. J. Robinson (2001), Melt generation at very slow-spreading oceanic ridges: Constraints from geochemical and geophysical data, *J. Petrol.*, *42*, 1171–1196, doi:10.1093/petrology/42.6.1171.

Wilson, D. S., et al. (2006), Drilling into gabbros in intact oceanic crust, *Science*, *312*, 1016–1020, doi:10.1126/science.1126090.

Zelt, C. A., and D. A. Forsyth (1994), Modeling wide-angle seismic data for crustal structure: Southeastern Grenville Province, *J. Geophys. Res.*, *99*, 11,687–11,704, doi:10.1029/93JB02764.

Zelt, C. A., and R. B. Smith (1992), Seismic traveltime inversion for 2-D crustal velocity structure, *Geophys. J. Int.*, *99*, 16–34, doi:10.1111/j.1365-246X.1992.tb00836.x.

Zelt, C. A., and B. C. Zelt (1998), Study of out-of-plane effects in the inversion of refraction/-angle reflection travel times, *Tectonophysics*, *286*, 209–221, doi:10.1016/S0040-1951(97)00266-7.

Zhang, T., J. Lin, and J. Y. Gao (2011), Interactions between hotspots and the Southwest Indian Ridge during the last 90Ma: Implications on the formation of oceanic plateaus and intra-plate seamounts, *Sci. China Earth Sci.*, *54*(8), 1177–1188, doi:10.1007/s11430-011-4219-9.

Zhang, T., J. Lin, and J. Y. Gao (2013), Magmatism and tectonic processes in the area of hydrothermal vent on Southwest Indian Ridge, *Sci. China Earth Sci.*, *56*, 2186–2197, doi:10.1007/s11430-013-4630-5.

Zhao, M. H., X. L. Qiu, J. B. Li, D. Sauter, A. G. Ruan, J. Chen, M. Cannat, S. Singh, J. Z. Zhang, Z. L. Wu, and X. W. Niu (2013), Three-dimensional seismic structure of the Dragon Flag oceanic core complex at the ultraslow spreading Southwest Indian Ridge (49°39′E), *Geochem. Geophys. Geosyst.*, *14*, 4544–4563, doi:10.1002/ggge.20264.

Zhou, H. Y., and H. J. B. Dick (2013), Thin crust as evidence for depleted mantle supporting the Marion Rise, *Nature*, *494*, 196–201, doi:10.1038/nature11842.